Dynamically Tunable Optical Cavities with Embedded Nematic Liquid Crystalline Networks

ADVANCED MATERIALS
www.advmat.de

Dynamically Tunable Optical Cavities with Embedded Nematic Liquid Crystalline Networks

Irina Zubritskaya, Rafael Cichelero, Ihar Faniayeu, Daniele Martella, Sara Nocentini, Per Rudquist, Diederik Sybolt Wiersma, and Mark L. Brongersma*

Tunable metal–insulator–metal (MIM) Fabry–Pérot (FP) cavities that can dynamically control light enable novel sensing, imaging and display applications. However, the realization of dynamic cavities incorporating stimuli-responsive materials poses a significant engineering challenge. Current approaches rely on refractive index modulation and suffer from low dynamic tunability, high losses, and limited spectral ranges, and require liquid and hazardous materials for operation. To overcome these challenges, a new tuning mechanism employing reversible mechanical adaptations of a polymer network is proposed, and dynamic tuning of optical resonances is demonstrated. Solid-state temperature-responsive optical coatings are developed by preparing a monodomain nematic liquid crystalline network (LCN) and are incorporated between metallic mirrors to form active optical microcavities. LCN microcavities offer large, reversible and highly linear spectral tuning of FP resonances reaching wavelength-shifts up to 40 nm via thermomechanical actuation while featuring outstanding repeatability and precision over more than 100 heating–cooling cycles. This degree of tunability allows for reversible switching between the reflective and the absorbing states of the device over the entire visible and near-infrared spectral regions, reaching large changes in reflectance with modulation efficiency $\Delta R = 79\%$.

1. Introduction

The metal–insulator–metal (MIM) geometry finds a wide range of applications in optics and enables everything from subwavelength waveguides[1–3] and perfect absorbers[4–7] to color filters[8,9] and spectrometers.[10] The growing need for devices capable of dynamically controlling optical responses in real time has prompted a renewed interest in asymmetric Fabry–Pérot (FP) cavities, also termed Gires–Tournois resonators. They are comprised of one optically thick and one optically thin metallic mirror through which light can enter the structure. These optical elements are known for their ease of fabrication and effectiveness in resonating and enhancing light–matter interaction at selected wavelengths.[4,6,7] The general strategy to achieve dynamic tuning in FP resonators is to replace the passive insulator that commonly sits between the mirrors by dynamically tunable materials such as graphene,[11–13] phase-change magnesium,[14] electro-optical polymers,[15] liquid crystals (LCs)[16–18] and conducting oxides[19–21] via the field-effect.[22] Several works showed that electrical gating of indium-tin-oxide incorporated in the cavity facilitates control over light absorption[12,19] and its reflection phase in mid-infrared[20] and near-infrared.[21] Other research exploited electrochromic oxide[23] and polymers[24–26] with nanostructures to tune the resulting reflected color. Researchers showed that optical pumping of gallium-doped zinc oxide[27] and alumina[28] allows for ultrafast modulation of cavity resonances in a sub-picosecond regime. Tuning can also be achieved in non-conventional ways by light pressure,[29] directed self-assembly of nanoparticles in a liquid electrolyte[30] and by phase-tunable meta-mirrors.[31] To reduce fabrication complexity, a large variety of responsive materials

I. Zubritskaya, M. L. Brongersma
Geballe Laboratory for Advanced Materials
Stanford University
476 Lomita Mall, Stanford, CA 94305, USA
I. Zubritskaya, R. Cichelero, I. Faniayeu
Department of Physics
University of Gothenburg
Origovägen 6B, Gothenburg 41296, Sweden
E-mail: irzu@gu.se
The ORCID identification number(s) for the author(s) of this article can be found under https://doi.org/10.1002/adma.202209152.

DOI: 10.1002/adma.202209152

D. Martella, S. Nocentini, D. S. Wiersma
European Laboratory for Non-Linear Spectroscopy (LENS)
University of Florence
via Nello Carrara 1, Sesto Fiorentino 50019, Italy
D. Martella, S. Nocentini, D. S. Wiersma
Istituto Nazionale di Ricerca Metrologica (INRiM)
Strada delle Cacce 91, Torino 10135, Italy
P. Rudquist
Department of Microtechnology and Nanoscience - MC2
Chalmers University of Technology
Kemivägen 9, Gothenburg 41296, Sweden
D. S. Wiersma
Physics and Astronomy Department
University of Florence
via G. Sansone 1, Sesto Fiorentino 50019, Italy

with tunable optical properties such as phase-change vanadium dioxide,[32] Zn–sodium vanadium oxide,[33] electrochromic polymers[34,35] and hydrogel[36] were proposed in lithography-free FP cavities. As new approaches continue to emerge, the vast majority of works still solely rely on modulation of refractive index and suffer from limited tunability, operation across a small spectral range and a need for liquid environments, making them unpractical for many applications. As an alternative, thickness-tunable polymeric materials and gels offer improved tunability but require liquids to swell and deswell, which reduces their application space.[36–39] Broad tuning of FP resonances was also achieved with nano-electromechanical (NEMS) devices,[40,41] but these tend to require quite sophisticated and thus costly fabrication.

In this work, we show that broad, dynamic tuning of FP resonances can be achieved mechanically without the need for liquids or NEMS processing by using a thermally responsive, nematic liquid crystalline network (LCN)[42–44] as the active layer of an MIM cavity. LCNs are elastic polymers with the molecular order of liquid crystals. They exhibit large and reversible mechanical deformation in response to different external stimuli such as temperature[45,46] and light,[47,48] making them attractive for soft actuators,[49–51] sensors,[52] artificial muscles,[45,53] soft robotics[50,54,55] and responsive coatings.[56,57] In addition, LCNs offer remarkable optical transparency at visible and near-infrared frequencies, and tunable birefringence.[58,59] The nematic LCN in our work is a stimuli-responsive material that displays the nematic liquid-crystalline phase within a cross-linked elastic polymer network. This nematic network is formed by acrylate-based mesogens (the LC molecules with rod-like structure) that are first aligned in the nematic phase and then simultaneously polymerized and cross-linked via photoactivated free radical polymerization.[60] Molecular interactions and perturbation in the orientational order of the mesogenic moieties stretch the polymer chains and can be harnessed to drive anisotropic mechanical deformation.[42,49] Dynamic tuning of our metal–LCN–metal FP cavities exploits temperature-induced reversible mechanical actuation of the LCN. When the temperature increases, the LCN undergoes a continuous transition from the ordered nematic to a less ordered paranematic state leading to a different polymer conformation and this results in fully reversible shape-adaptations via mechanical actuation.[42,49,59,61] The original shape is fully recovered when the thermal stimulus is removed. In contrast to other mechanically responsive materials, for example, shape-memory polymers and gels, the mechanical deformation of our LCN is anisotropic and depends on the molecular alignment and internal strain in the polymer network. In the following sections, the synthesis and dynamic optical properties of LCN cavities will be discussed in detail and their large spectral tuning will be highlighted.

2. Results and Discussion

2.1. Preparation of Liquid Crystalline Network Optical Coatings and Cavities

Herein, we demonstrate the previously unexplored optical and mechanical properties of nematic LCN optical coatings and cavities prepared on metallic substrates. We obtain LCN of excellent optical quality by adopting general approaches to prepare macroscale films and cells for photolithography.[62–66] Our synthetic strategy relies on photopolymerization of mesogens bearing acrylate groups using the photoinitiator Irgacure 369 (**Figure 1**a). To prepare LCN optical coatings and microcavities, we combine low molecular weight LC monoacrylate monomer 1 (C6BP) and diacrylate monomer 2 (RM257) acting as a cross-linker (Figure 1a). The nematic-isotropic phase transition temperature of the LC monomers is around 65 °C, and the nematic phase remains stable in the temperature range 22–45 °C in thin films. The mixture is first infiltrated in its isotropic phase at 120 °C in a cell made from aluminum (Al)–coated glass and bare glass substrates, then aligned in the liquid crystalline nematic phase at 45 °C by using a slow cooling and annealing. Finally, the mixture is polymerized by ultraviolet (UV) irradiation at room temperature (RT) to form a solid polymer network that retains the initially established liquid crystalline nematic order (Figure 1b and Figure S1, Supporting Information). This LCN layer serves as the active medium in a planar Al–LCN–Al cavity that is formed by removing the top glass and depositing a top Al mirror (Figure 1b). One of the Al layers in the Al–LCN–Al cavity is made sufficiently thick to be fully reflective and the other is thinner and semi-transparent. It is crucial to establish a uniform molecular orientation in the LCN in order to achieve a well-defined and reproducible optical response under stimuli. Whereas polydomain LCN coatings can still produce some level of mechanical transformations,[67] the presence of multiple domains in films results in unwanted scattering losses and non-uniform optical properties. This can be seen in optical and cross-polarized optical images in Figure 1c (top panel). In this work, we maximize the mechanical and optical responses by establishing monodomain homeotropic molecular alignment (molecules oriented perpendicular to the surface) leading to out-of-plane optical and mechanical anisotropy of the films.

The optical and cross-polarized optical microscopy images of nematic monodomain LCN coatings on an Al substrate are shown in Figure 1c (central panel). In contrast to the polydomain LCN, the aligned monodomain LCN coating displays uniform optical properties and is transparent[58] thanks to a suppression of fluctuations in the LC director (Figure S2, Supporting Information).[42] The Al–LCN–Al cavity shows how multiple colors can be achieved through the thin film interference effects with a varying cavity thickness across the sample (Figure 1c [bottom panel], and Figures S3 and S4, Supporting Information). Given the small lateral gradient in the cavity thickness of 0.2 μm mm^{-1}, each region can be viewed as an independent cavity with a well-defined mirror spacing. As such, the cavity behavior can be conveniently analyzed for different mirror spacings. Homeotropic alignment and out-of-plane optical anisotropy in the coating and cavity is verified by taking cross-polarized reflection images (Figure 1c (central and bottom panels), and Figures S2–S4, Supporting Information), which remain dark upon rotating the sample by 45°. We obtain the ordinary and extraordinary refractive indices by fitting the spectroscopic ellipsometry data taken from a LCN layer (Figure S8 and S9, Supporting Information) to a birefringent Cauchy model (Figure S7, Supporting Information).[68] For the ellipsometry, we prepare homeotropic LCN coatings on a silicon substrate (Figure S5, Supporting Information) and measure the thickness of the homeotropic region used in the ellipsometry analysis by atomic force microscopy (AFM) (Figure S6, Supporting Information).

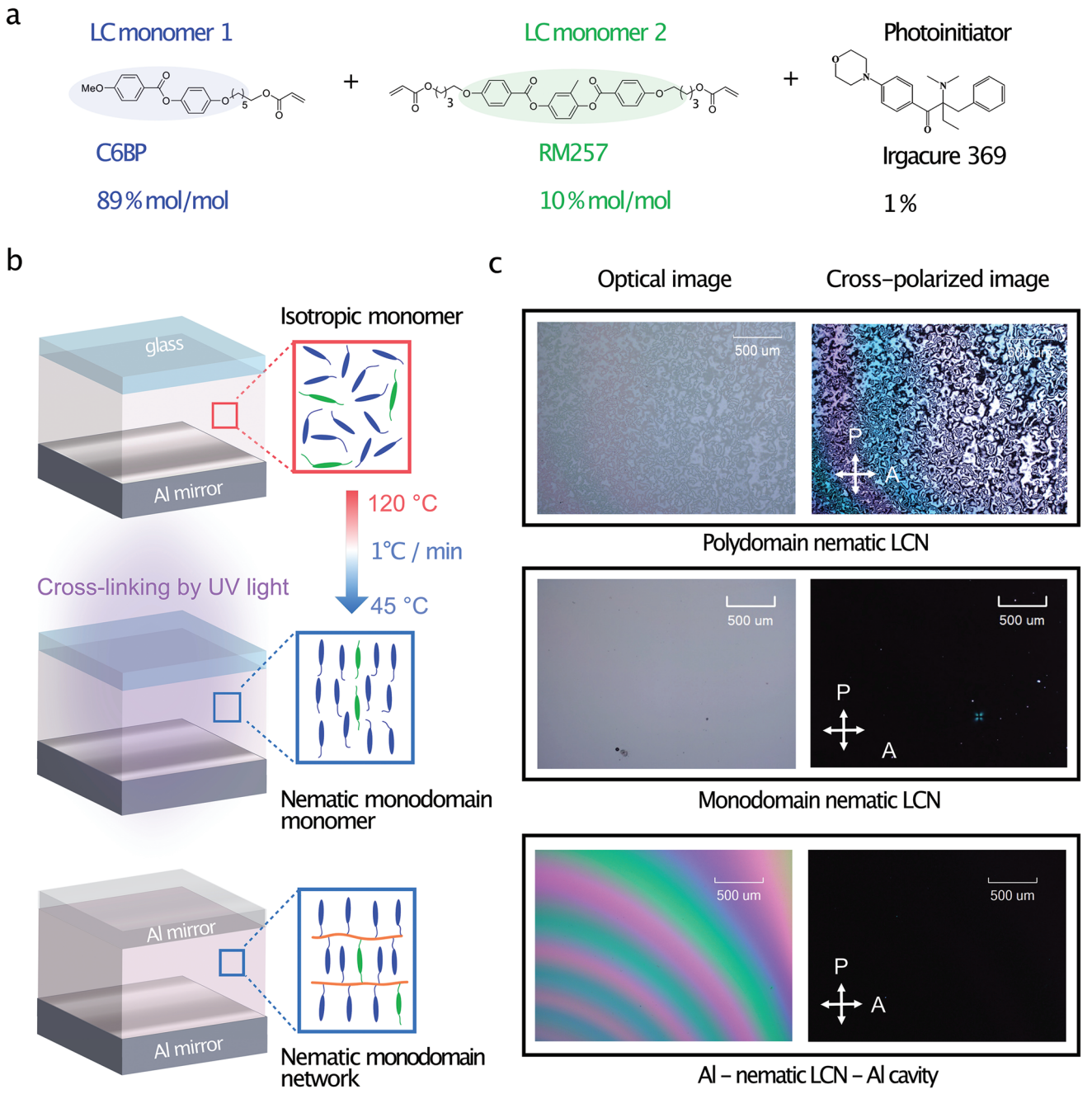

Figure 1. Correlation between the molecular structure and optical properties of the prepared liquid crystalline network (LCN) optical coatings and cavities. a) Components of the LCN and their molecular structure. b) Main preparation steps of optical layers in an Al–nematic LCN–Al cavity. c) Optical (left) and cross-polarized (right) optical microscopy images of obtained polydomain (top panel) and monodomain homeotropic (central panel) LCN layer on an Al substrate. The bottom panel shows such images of an Al–LCN–Al cavity with homeotropic alignment. The arrows indicate the orientation of the polarizer and analyzer in the cross-polarized images.

2.2. Optical Response of LCN Microcavities and Effect of Mechanical Actuation on Their Resonant Properties

We investigate the resonant behavior of optical microcavities made of aluminum (Al) mirrors and vertically aligned nematic LCN (**Figure 2**a,b) illuminated at normal light incidence. In the following discussion, we will refer to these cavities as thin and thick where the LCN thickness is, respectively, 830 and 2630 nm. We chose these thicknesses to conveniently analyze how thermomechanical actuation of LCN modifies the resonant optical properties of FP cavity devices with different numbers of supported modes and *Q*-factors. Optical reflectance spectra in the visible and near-infrared ranges obtained at RT before actuation are presented in Figures 2a (top) and 2b (top) in dark blue. The observed reflectance minima (near-zero reflection) at selected wavelengths can only be obtained if the sum

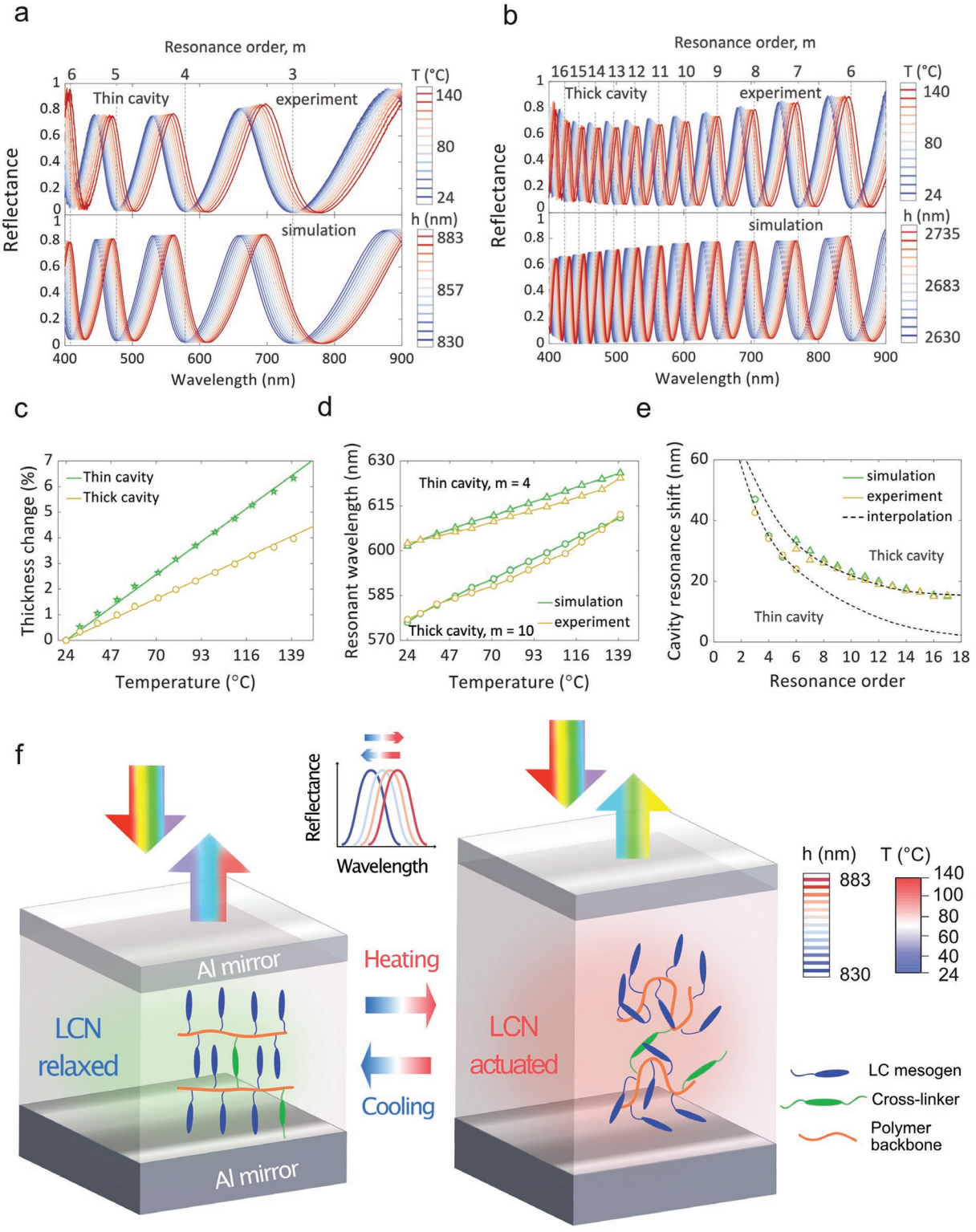

Figure 2. a,b) Experimental (top) and calculated (bottom) reflectance spectra of Al–LCN–Al cavities with a thin (830 nm) (a) and a thick (2630 nm) (b) LCN layer obtained for different temperatures and thicknesses, respectively. c) Calculated relative thickness change at 140 °C in thin and thick cavities. d) The experimental and calculated effect of thermal actuation on the resonant wavelength of two spectrally close resonances in thin and thick cavities. e) Experimental and calculated spectral shifts of cavity resonances resulting from a temperature change from room temperature to 140 °C in the thin and thick cavities. f) Mechanism of tuning of resonant optical properties in optical Fabry–Pérot cavity with integrated active LCN layer showing the molecular structure of our nematic LCN and thermally induced changes in the molecular order and thickness. Insets illustrate reversible changes in cavity thickness and the resonant wavelength with temperature.

of reflected waves r_0, r_1, ... r_n approaches zero, where r_0 is the reflection amplitude of the directly reflected wave and r_1, r_2, ... r_n are the partially reflected light waves resulting after travelling one, two, ... n round-trips in the cavity.[7,69] The condition for destructive interference in an asymmetric FP resonator can be derived from Airy formula for the reflection coefficient:[69]

$$r_{\text{Total}} = \frac{r_{\text{Top}} - r_{\text{Bottom}} e^{2i\beta h_{\text{LCN}}}}{1 - r_{\text{Top}} r_{\text{Bottom}} e^{2i\beta h_{\text{LCN}}}} \quad (1)$$

where r_{Top} is the reflection from the top mirror, r_{Bottom} is the reflection from the bottom mirror, and $\beta = (2\pi/\lambda)n_{\text{LCN}}$ is the longitudinal wavenumber in the cavity, and h_{LCN} and n_{LCN} are the thickness and the ordinary refractive index of the homeotropically aligned LCN layer. The condition is met when the numerator in the Equation (1) vanishes[69] such that $r_{\text{Top}} - r_{\text{Bottom}} e^{2i\beta h_{\text{LCN}}} = 0$. The cavity in Figure 2a (top) reveals fewer resonant orders (dips) as compared to the cavity in Figure 2b (top), indicating a smaller thickness. To retrieve thicknesses of the LCN in the thin and thick cavities and the orders of supported resonant modes, we numerically model the reflectance at normal incidence to reproduce the experimental spectra by using a finite element method to solve Maxwell's equation[70] (COMSOL Multiphysics, Wave Optics module). The resulting calculated spectra are shown in Figure 2a,b (bottom), where the retrieved thicknesses are given in dark blue on the right, and the resonance orders are shown on the top. We show the full reflectance spectra including the zeroth-order FP mode spanning from the visible to the mid-infrared of the thin and thick cavities in Figure S10a,b, Supporting Information.

In the next step, we investigate the effect of thermomechanical actuation of LCN on the resonant properties of these Al–LCN–Al optical cavities. In Figures 2a (top) and 2b (top), we show the experimental spectra of the thin and thick cavities recorded as the temperature is increased from RT to 140 °C with 10 °C incremental steps. In both optical cavities, we observe a redshift of the resonant peaks, revealing an increase in the optical thickness $h_{\text{LCN}}n_{\text{LCN}}$, where the magnitude of the shift is proportional to the actuation temperature, resulting in ≈40 nm spectral shifts at 140 °C. It is generally non-trivial to distinguish the relative contributions from the actual thickness change Δh_{LCN} and the refractive index change Δn_{LCN} to the change in optical thickness $\Delta(h_{\text{LCN}}n_{\text{LCN}})$. To elucidate this behavior, we first analyze how changes in the LCN thickness affect the reflectance spectra of the thin and thick cavities. We perform a parametric scan for different thicknesses (Figure S11a,b, Supporting Information) to reproduce the experimental spectra at each temperature as shown in Figures 2a (bottom) and 2b (bottom). By matching the experiment and simulation, we establish that the observed redshifts of the resonant peaks are associated with a linear increase in thickness from 830 to 883 nm in the thin cavity, and from 2630 to 2735 nm in the thick cavity.

In Figure 2d, we highlight the effect of actuation for two selected resonant modes that are spectrally close but have different orders in the thin and thick cavities. We show by experiment and simulation how the resonant modes with $m = 4$ in the thin cavity (Figure 2a) and $m = 10$ in the thick cavity (Figure 2b) evolve with temperature. First and foremost, we notice a clear linear dependence in the resonant peak shift with temperature. Both cavities show comparable peak shifts at 140 °C regardless of the LCN thickness. This indicates that the thermomechanical response is critically linked to the initial LCN layer thickness. In Figure 1e, we show the experimental spectral shift of cavity resonances $\Delta\lambda = \lambda_m$ (140 °C) − λ_m (RT), where λ_m (RT) and λ_m (140 °C) are the spectral positions of the resonance m at RT and 140 °C, followed by their respective numerical simulations. Both experiment and simulation show a clear and expected trend, where low-order resonances exhibit larger spectral shifts. This can be explained by the quadratic wavelength dependence of the free spectral range $\Delta\lambda_{\text{FSR}}$ (spectral separation between the resonant wavelengths), as shown in Equation (2):[71]

$$\Delta\lambda_{\text{FSR}} \approx \frac{\lambda^2}{2h_{\text{LCN}}n_{\text{LCN}}} \quad (2)$$

The maximal shifts are obtained for the fundamental cavity resonance at longer wavelengths, whereas for the high-order resonances at shorter wavelengths the shifts become smaller.

2.2.1. The Actuation Mechanism for Tuning of the Resonant Properties of LCN Microcavities

We directly probe the thermally induced mechanical change in LCN thickness with AFM by performing scans at RT and at 130 °C by considering a homeotropically aligned LCN film with a 1 µm thickness on an Al-coated substrate with a 3 nm Cr adhesion layer as in the cavities (Figure S14, Supporting Information). We find that there is a 10% increase in the thickness at 130 °C, which is consistent with our optical measurements. Due to a less constrained geometry and the absence of the top mirror, the mechanical actuation generated at the edge of this LCN film can be larger compared to the regions away from the edge. To gain insight into the contribution of the refractive index, we analyze how its variation can affect the resonant optical properties. For the vertically aligned LCN with out-of-plane optical anisotropy that we have created, the normally incident light only senses the ordinary (in-plane) refractive index n_o. We numerically model the spectral response of Al–LCN–Al cavities assuming that only n_o varies with increasing temperature while the cavity thickness remains constant (Figure S12, Supporting Information). We find that in order to achieve same cavity resonance shifts at 140 °C, the change in the ordinary refractive index n_o must reach the values of $\Delta n_o = 0.095$ and $\Delta n_o = 0.06$ (or 6% and 4% for the thin and thick cavities). These values are rather unrealistic for our cross-linked LCN. The small effect of thermal actuation on the refractive index of acrylate-based LCNs was previously discussed in the literature.[59,61,72] Martella et al. showed that a significant amount of optical anisotropy can be maintained by our cross-linked LCN after heating to at least 150 °C and a complete nematic–isotropic phase transition is not observed by heating up to 200 °C.[65] Previous work of De Bellis et al. reported a small non-linear decrease in optical anisotropy upon heating to 130 °C accompanied by a 0.3% increase in the ordinary refractive index at telecom wavelengths in our LCN.[64] Our observations are consistent with these works, where the increasing

temperature decreases the nematic order in the network and reduces the optical anisotropy. We note that a small refractive index variation $\Delta n_o = 0.005$ (0.3%) has a negligible effect on the resonant properties of the cavities (Figure S12a,c, Supporting Information). Even for $\Delta n_o = 0.019$ or 1.22%, and $\Delta n_o = 0.012$ or 0.8% changes (higher than the reported values), we obtain peak shifts of 7 and 4 nm at the resonant orders of 4 and 10 in the thin and thick cavities (Figure S12a,c, Supporting Information) that are too small to explain the experimentally observed shifts. By varying the thickness h and the refractive index simultaneously, we find that matching the experiment requires unrealistic values of $\Delta n_o = 0.04$ or 2.6%, and that the thickness change is non-consistent with our AFM measurements (Figures S12e,f and S14, Supporting Information). If $\Delta n_o = 0.005$, similar thickness variation as shown in lower panels of Figure 2a,b is obtained. The linear dependence of resonant peak shifts with temperature (Figure 2c) further suggests that the refractive index that varies non-linearly with temperature in this temperature range[64] has a minor contribution to tuning. These findings indicate that the dominant tuning mechanism of the optical FP microcavities can be attributed to the thermomechanical response of the LCN, which is linear with temperature.[73] We note that the refractive-index changes only have a minor contribution to the tuning of the spectral responses in low-Q optical cavities, while more notable contributions can be expected in high-Q microcavities.[74]

Having shown that the thermomechanical response of LCN provides the dominant contribution to the observed changes in the resonant properties of optical cavities, we evaluate the effect of mechanical actuation on the calculated changes in LCN thickness (Figure 2a,b [bottom]), reflecting an outstanding linear response to temperature (Figure 2c). At 140 °C, the relative thickness change defined as $(h_{140} - h_{RT})/h_{RT} \times 100\%$, where h_{RT} and h_{140} are the thicknesses at RT and 140 °C, reaches the values 6.5% and 4% in the thin and thick cavities, respectively, that are consistent with previous studies[55] if the confinement by the substrate is taken into account. The reported values for linear thermal expansion coefficients of isotropic acrylate-based nematic networks are below 2×10^{-4} °C^{-1}, or 2% at 140 °C,[73,75] indicating that the thickness change in Al–LCN–Al cavities is attributed to mechanical actuation of aligned LCN rather than ordinary thermal expansion. Because the linear thermal expansion coefficient of borosilicate glass[76] is two orders of magnitude lower than that of LCN, the contribution of substrate is negligible.

The working mechanism of the dynamic optical cavity with a nematic LCN active layer incorporated between Al mirrors is presented in Figure 2f. The thermally induced loss of molecular order results in mechanical actuation of the LCN and a thickness-change, which in turn modifies the resonance condition of the Al–LCN–Al cavity and spectrally shifts the resonances. The increase in thickness in our vertically aligned nematic network is rather unusual because LCN formed by similar mesogens typically display a contraction along their molecular director,[55,77,78] suggesting a prolate conformation of their polymer backbone.[49] However, the increase in thickness can be explained by an oblate conformation due to the presence of strain in the as-synthesized films and thin-film geometry. The majority of works study free-standing macroscopic LCN and little is known about thermomechanical behavior of optically thin monodomain nematic LCN coatings. In multidomain coatings where the lateral deformation is restricted by a rigid substrate, the anisotropic deformations act simultaneously in the vertical direction.[67,79] Since our LC monomer coats the substrate at high temperature by capillary action followed by cooling to the nematic phase and cross-linking, the resulting LCN coating is pre-strained. Moreover, previously discussed anisotropic shrinkage[73] and photopolymerization temperature[80] of nematic networks could lead to additional internal strain in our thin, vertically aligned LCN coatings. Because of in-plane (i.e., tensile) strain, polymer chains tend to align parallel to the substrate in thin films.[81] A significantly different interaction of LC mesogens and the polymer backbone can be expected in the thin film configuration. In our case, the tensile strain forces the polymer chains to align parallel to the substrate while the mesogens are aligned homeotropically due to the strong anchoring conditions. Homeotropic nematic order and strain in the polymer chains lead to an LCN with an oblate chain conformation[49] where the polymer backbone lies in plane perpendicular to the mesogens (Figure 2f). In this situation, the increasing temperature releases the internal strain and decreases the nematic order in LCN, leading to an out-of-plain deformation and an increase in thickness. Previous works demonstrated that our mesogens can form a LCN with an oblate conformation of polymer chains[82] that expands along the LC director upon heating. It is clear that tensile strain relaxation and the loss of nematic order upon heating both contribute to the observed expansion in our vertically aligned elastic network. Whereas our explanation is consistent with the observation of film expansion, future studies can benefit from further materials characterization that directly probes the structural changes in the LCN.

2.2.2. Dynamic Tuning of Resonant Wavelength of Optical Microcavity

We evaluate in detail the dynamic optical properties offered by our Al–LCN–Al cavities, specifically focusing on the parameters such as amplitude modulation, reproducibility, linear response and precision that are relevant for tunable device applications. Based on Figure 2b, we particularly investigate dynamic changes in the reflectance R at selected wavelengths and obtain absolute modulation efficiency $\Delta R = R_{140} - R_{RT} = 78\%$ at 850 nm ($m = 6$), 79% at 770 nm ($m = 7$), 74% at 705 nm ($m = 8$), 68% at 650 nm ($m = 9$), 61% at 603 nm ($m = 10$) and 56% at 563 nm ($m = 11$), where R_{140} and R_{RT} are the reflectances at 140 °C and at RT. The presented cavities maintain sizable tunability and modulation efficiencies at oblique angles of incidence but become polarization-sensitive (Figures S11, S13, and S17, Supporting Information). Consequently, the near-zero reflectance cannot be achieved because the efficiency of coupling to the FP resonant modes decreases at oblique incidence. We observe a linear redshift with increasing thickness in the reflectance spectra for s- and p-polarized light at oblique angles of incidence (Figures S11 and S17, Supporting Information). For the same cavity thickness, the reflectance for the s- and p-polarized light behaves similarly at small incidence angles below 30° but

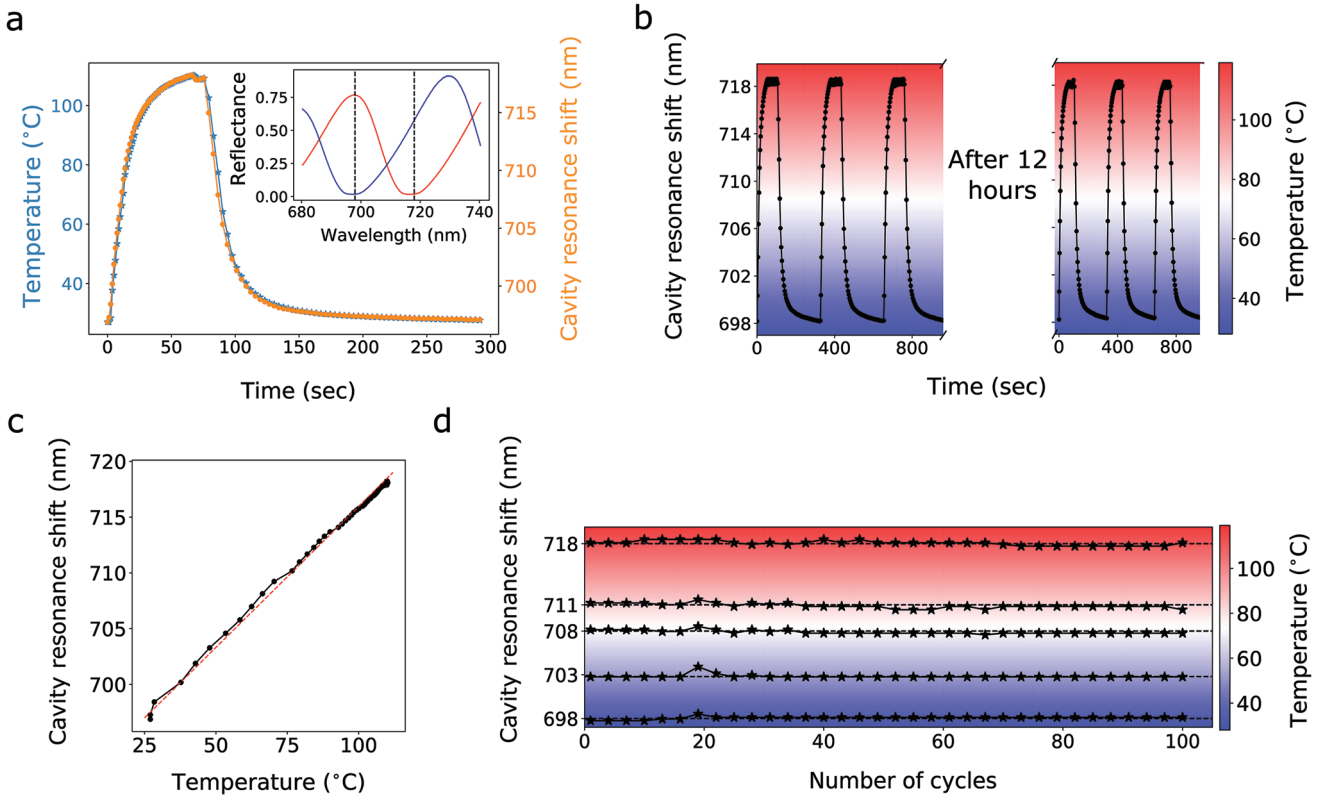

Figure 3. The evolution, reproducibility and linearity of the spectral tuning of thermally activated Al–LCN–Al cavity. a) Evolution of the heater temperature (left *y*-axis) and the resulting cavity resonance shift $\Delta\lambda$ (T) (nm) (right *y*-axis) during a full thermal cycle, in which the temperature is raised from RT to 110 °C and lowered back to RT. Inset: switching between the states with the lowest and highest reflectance at the wavelength of 698 nm. b) Cavity resonance shift $\Delta\lambda$ (T) obtained during 150 thermoelastic cycles. c) Temperature dependence of the cavity resonance shift (red dashed line–linear fit). d) Cavity resonance shifts $\Delta\lambda$ (T) obtained at different set temperatures during 100 cycles. The background color in (b) and (d) reflects the temperature scale as quantified on the right *y*-axes.

diverges dramatically under oblique incidence angles above 40° (Figure S13, Supporting Information). We also observe that the resonant modes blueshift as the incidence angle increases and that polarization conversion is not present (Figure S18, Supporting Information).

Finally, we demonstrate the dynamic response of our cavities, highlighting their significant thermoelastic response and reproducibility in **Figure 3**. To highlight these features, we select the spectral region from (680–740 nm) of the cavity in Figure 1b showing the resonance with $m = 8$ at a wavelength of 698 nm at RT (inset in Figure 3a). In Figure 3a, we simultaneously track how the position of the resonance (in orange) evolves with temperature and time along with the applied temperature (in blue). A full thermal cycle consists of heating from RT to 110 °C (initial 60 s) and passive cooling down to RT (time interval from 60 to 300 s). We use the operation temperature of 110 °C, which is sufficient for switching between the states with lowest and highest reflectance at a wavelength of 698 nm as presented in the inset to Figure 3a. Figure 3c features a strikingly linear response of the spectral shift to temperature, thus making Al–LCN–Al cavities ideal for tunable device applications. We emphasize that the thermomechanical response of the optical cavity strictly follows the temperature. The response time of LCN in the present work is only limited by the response time of the hotplate and heat sinking capabilities; thus, improving these parameters can result in a faster response. For instance, using light as a local stimulus allows one to reach response time on a scale of a few milliseconds.[77] Alternatively, a faster response and active tuning can be achieved with voltage-controlled microheaters.[83]

We subject the thermomechanically active Al–LCN–Al cavity to over 150 thermomechanical cycles with similar parameters as presented in Figure 3a. The spectral behavior of the eighth-order resonance ($m = 8$) with respect to temperature over time is presented in Figure 3b, where the background color reflects the temperature scale. The first three thermal cycles are shown in the left panel, while the right panel shows the fully reversible thermal response after 720 min of continuous thermomechanical actuation and relaxation, resulting in a highly reproducible behavior with no signs of degradation of the LCN and no significant changes in the surface morphology. After 130 thermomechanical cycles, no cracking or delamination was observed but surface graininess slightly increased (Figure S15, Supporting Information). The resonant optical properties of the Al–LCN–Al cavity were fully preserved after 130 cycles, which serves as an excellent marker of the device stability. This shows that the top Al was not oxidized and, in fact, may contain a few nanometers of protective alumina.

Furthermore, we investigate the precision of spectral tuning by plotting the spectral shift $\Delta\lambda$ of the eighth-order resonance

at chosen temperatures over 100 cycles as shown in Figure 3d. We notice that the dynamic mechanical changes in the cavity at RT, 50, 70, 82 and 110 °C can controllably tune the resonances with sub-nanometer precision to 698, 703, 708, 711 and 718 nm, respectively, which is fully consistent over 100 cycles of actuation and relaxation, as indicated by the dashed lines. Similar linear response, reproducibility and stability of thermomechanical tuning is achieved for over 130 thermomechanical cycles at 60° angle of incidence as shown in Figure S16, Supporting Information.

3. Conclusions

We have developed thermomechanically responsive optical coatings with a nematic LCN that we further incorporated in the most fundamental photonic structure—a MIM FP optical cavity—as an active cavity layer. By sandwiching the nematic network between two Al mirrors, we demonstrate a new way to dynamically tune optical resonances in a solid-state optical microcavity device that operates via thermomechanical transformations in the nematic network. Importantly, due to the solid-state operation and outstanding optical quality, LCN microcavities offer improved levels of tuning via large thermally induced thickness changes, adding to the spectrum of previously reported dynamic cavities based on phase-change materials, electrochromic polymers and hydrogels. Particularly, large reflection modulation ΔR can be achieved for several-micrometer-thick cavities due to the high optical transparency of the LCN. The active microcavities exhibit large reversible and continuous spectral tuning of the FP resonances across the entire visible and near-infrared spectral ranges, reaching shifts up to 40 nm and absolute modulation efficiencies ΔR up to 79%. The linear dependence of the resonant reflectance with temperature can be desirable for a variety of applications, including, for example, tunable filters, laser cavities and display. The presented devices offer thermoelastic response times on the order of a few tens of seconds, while maintaining outstanding mechanical stability and reproducibility of placing cavity resonance with sub-nanometer accuracy over at least 100 thermoelastic actuation–relaxation cycles. We emphasize that stability and reproducibility of that level have not been previously reported in dynamic FP cavities based on soft materials. Comparing with the reported non-thermal FP cavities, the primary advantages of LCN cavities are their solid nature, large absolute modulation ΔR, broad range of operation wavelengths spanning over the entire visible and near-infrared, and stability and precision of dynamic tuning. The limiting factor of LCN, compared with ultrafast all-optically and gate-tunable nano-cavities, is their relatively slow response due to the intrinsic dynamics of thermal relaxation. Further improvements of LCN-activated optical cavities can be achieved by precisely controlling the LCN thickness, for instance using laser writing and grayscale lithography. Phase-gradient novel dynamic coatings and cavities can be obtained by exploiting more complex alignment of mesogens, including spatially varying the birefringence axis using photoalignment.

4. Experimental Section

Preparation of LC Monomer Mixtures: LC monomers were purchased from Synthon Chemical, while the photoinitiator Irgacure 396 was purchased from Sigma-Aldrich and used as received. The monomer mixture was prepared by mixing the monoacrylate liquid crystal C6BP (4-methoxybenzoic acid 4-(6-acryloyloxyhexyloxy) phenyl ester, 89% mol mol^{-1}), the cross-linker RM257 (4-bis-[4-(3-acryloyloxypropyloxy)-benzoyloxy]-2-methylbenzene, 10% mol mol^{-1}) and the photoinitiator Irgacure 369 (1% mol mol^{-1}). All components were homogeneously mixed in dichloromethane, followed by evaporation of the solvent.

Preparation of Optical LCN Coatings and Al–LCN–Al Cavities: The fabrication process flow is shown in Figure S1, Supporting Information. A polymerization cell that consisted of a metallic substrate and a top borosilicate glass promoting homeotropic alignment were exploited. Borosilicate glass substrates (Menzel Gläser) were cleaned by ultrasonication for 5 min in acetone, 5 min in isopropanol, and 5 min in DI water. Next, 100 nm of aluminum was deposited followed by 3 nm of chromium at a rate 2 Å s^{-1}. It was found that 3 nm of chromium significantly improved adhesion and wettability of the LCN on aluminum. The subsequent preparation steps were carried out in yellow light to avoid unwanted UV exposure. The metallic substrate was heated and annealed for 5 min at 120 °C; the LC monomer mixture was dispensed and it was let to fully melt. After melting, a cell was assembled by placing the borosilicate glass atop the monomer and it was let to uniformly coat the substrate by capillary tension. Next, the LC monomer was cooled down to 45 °C at a rate of 1 °C min^{-1} and annealed for 30 min to produce a monodomain nematic phase. The low surface energy of hydrophobic borosilicate glass that required no additional treatment to impose homeotropic alignment was taken advantage of. The homeotropic alignment was confirmed by polarized optical microscopy and then the monomer was exposed to UV light from a fluorescent lamp (365 nm, 80 mW cm^{-2}) for 10 min at RT to induce the photopolymerization. After that, the cell was soaked in deionized water for 1 h to facilitate detachment of the top glass. Next, the top glass was removed by opening the cell with a surgical blade and the resulting optical coating was dried in a nitrogen flow. Finally, the metal–LCN–metal FP cavities were constructed[6] by placing the LCN between two Al mirrors. For operation in reflection, the top mirror was made semi-transparent by depositing 10 nm of Al, which allowed for light circulation in the cavity loaded with the LCN. Importantly, previous studies showed that coating of LCNs with thin metallic layers did not compromise the actuation.[84]

Characterization of Optical Properties of the Liquid Crystalline Network: In order to obtain the birefringent optical constants of the LCN, the LCN was fabricated with homeotropic alignment on a silicon substrate (Figure S5, Supporting Information). Silicon was chosen as a substrate due to the well-known and consistent optical properties and smooth surface. The thickness was measured by AFM (Figure S6, Supporting Information) and was used in the ellipsometry model. The anisotropic optical properties of LCN were characterized by variable angle spectroscopic ellipsometry in the spectral region from 350 nm to 1 µm using the ellipsometer M2000 and software V-VASE (J.A. Woollam). The experimental ellipsometry data was collected by using three different angles of incidence, namely 65°, 70°, and 75°. The ordinary and extraordinary refractive indices were obtained by fitting the experimental ellipsometry data (Figure S8, Supporting Information) to a uniaxial, birefringent Cauchy model (Figure S7, Supporting Information) and using the measured AFM thickness (Figure S6, Supporting Information).

Finite Element Method Modeling: Full-wave numerical simulation of the reflectance spectra was carried out using commercial software (COMSOL Multiphysics, Wave Optics module). A 2D model with periodic boundary conditions and two ports as a source of plane wave illumination under normal and oblique incidence was used. The wavelength-dependent reflectance was calculated using the S-parameters. The square-mesh size used was set at 2×2 nm^2. To ensure realistic simulation results, the

previously reported refractive index for Al was used,[85] in which ultrathin films of Al were characterized. For the LCN, the experimentally obtained refractive index measured by spectroscopic ellipsometry was used (see Supporting Information).

Spectral Characterization of Optical Cavities: Reflectance spectra of optical cavities were acquired using a home-built set-up consisting of a fiber-coupled UV–visible–NIR halogen light source (HL2000, Ocean Optics), a high-OH UV–vis optical fiber with 600 µm core diameter (Ocean Insight). The light in all experiments was unpolarized. The collimated light beam was gently focused on the cavity by a 10x objective with a numerical aperture (Olympus Plan Fluorite Objective, 0.3 NA, 10 mm WD) producing a spot size of 300 µm. To precisely position the beam spot in different regions of cavities and collect reflectance spectra at different thicknesses, a 25.0 mm *XYZ* Translation Stage with Standard Micrometers was used. The spectra were collected at normal incidence for all temperatures starting from RT and increasing the temperature with a 10 °C step up to 130–140 °C. For a reference measurement of the reflectance, an Al mirror and an Ag mirror were used. For temperature measurements, a metal ceramic heater, a 100 Ω platinum resistance temperature detector (TH100PT, Thorlabs) and a PID temperature controller (TC200-EC, Thorlabs) were used. Thermally conductive adhesive tape was used to fix the sample on the ceramic heater. The optical spectra were recorded by a visible–NIR spectrometer (Ocean optics FLAME-VIS-NIR-ES) using an acquisition time of 3 ms and 50 accumulations. All spectral measurements and automated temperature measurements were performed using home-built software (LabView).

Supporting Information

Supporting Information is available from the Wiley Online Library or from the author.

Acknowledgements

This work was supported by the Knut and Alice Wallenberg Foundation postdoctoral fellowship (Award 2017.0466) and the Carl Trygger Foundation (Award CTS 20:495). Alexander Friemann Dmitriev is kindly thanked for offering his lab for optical measurements. Tom Carver (Stanford Nano Shared Facilities) is kindly thanked for his assistance in the clean room. Alexander Friemann Dmitriev, Ravi Shankar, Mohsen Tabrizi and Mohammad Taghinejad are kindly thanked for valuable discussions. Gervasi Herranz is kindly thanked for help with preparing the manuscript. Lu Di is kindly thanked for help with assembling the heater. James Hillfiker (J.A. Woollam) is kindly thanked for help with the ellipsometry model. Part of this work was funded by a DMREF/Collaborative Research program from the NSF (Award # 1921842). Part of this work was performed using the Swedish Research Infrastructure for micro- and nanofabrication Myfab and MC2 nanofabrication facility at Chalmers. Part of this work was performed at the Stanford Nano Shared Facilities (SNSF), supported by the National Science Foundation under award ECCS-2026822.

Conflict of Interest

The authors declare no conflict of interest.

Author Contributions

I.Z. designed and managed the project. I.Z., R.C., I.F., S.N., D.M., D.S.W. and M.L.B. conceived the concept. I.Z. fabricated and characterized optical coatings and cavities. I.Z., R.C., and I.F. designed and performed optical experiments and analyzed the data. R.C. built optical setup, wrote LabView codes and performed automated time-resolved measurements. I.F. performed finite-element method simulations and fitting of experimental data. D.M. and S.N. contributed to material preparation. P.R. contributed to thermal measurements and polarized microscopy, and provided useful insights on the material properties. I.Z. wrote the main manuscript. All authors participated in the discussions and contributed to the manuscript.

Data Availability Statement

The data that support the findings of this study are available in the Supporting Information of this article.

Keywords

dynamic tuning, elastomers, Fabry–Pérot cavities, liquid crystalline networks, metal–insulator–metal resonators, stimuli-responsive polymers, tunable optical cavities

Received: October 4, 2022
Revised: November 21, 2022
Published online:

[1] W. L. Barnes, A. Dereux, T. W. Ebbesen, *Nature* **2003**, *424*, 824.
[2] R. Zia, M. D. Selker, P. B. Catrysse, M. L. Brongersma, *J. Opt. Soc. Am. A* **2004**, *21*, 2442.
[3] F. Kusunoki, T. Yotsuya, J. Takahara, *Opt. Express* **2006**, *14*, 5651.
[4] M. Yan, *J. Opt.* **2013**, *15*, 025006.
[5] S. Shu, Z. Li, Y. Y. Li, *Opt. Express* **2013**, *21*, 25307.
[6] B. J. Lee, Z. M. Zhang, *J. Appl. Phys.* **2006**, *100*, 063529.
[7] A. T. Doan, T. D. Dao, S. Ishii, T. Nagao, *Opt. Express* **2019**, *27*, A725.
[8] Z. Li, S. Butun, K. Aydin, *ACS Photonics* **2015**, *2*, 183.
[9] K.-T. Lee, S. Seo, L. J. Guo, *Adv. Opt. Mater.* **2015**, *3*, 347.
[10] G. d. G. J. H. Correia, S. H. Kong, M. Bartek, R. F. Wolffenbuttel, *Sens. Actuators* **2000**, *82*, 191.
[11] M. Engel, M. Steiner, A. Lombardo, A. C. Ferrari, H. V. Lohneysen, P. Avouris, R. Krupke, *Nat. Commun.* **2012**, *3*, 906.
[12] Y. Yao, R. Shankar, M. A. Kats, Y. Song, J. Kong, M. Loncar, F. Capasso, *Nano Lett.* **2014**, *14*, 6526.
[13] V. Caligiuri, A. Pianelli, M. Miscuglio, A. Patra, N. Maccaferri, R. Caputo, A. De Luca, *ACS Appl. Nano Mater.* **2020**, *3*, 12218.
[14] Y. Chen, X. Duan, M. Matuschek, Y. Zhou, F. Neubrech, H. Duan, N. Liu, *Nano Lett.* **2017**, *17*, 5555.
[15] J. Zhang, Y. Kosugi, A. Otomo, Y.-L. Ho, J.-J. Delaunay, Y. Nakano, T. Tanemura, *Appl. Phys. Lett.* **2018**, *113*, 231102.
[16] S. Mansha, P. Moitra, X. Xu, T. W. W. Mass, R. M. Veetil, X. Liang, S. Q. Li, R. Paniagua-Dominguez, A. I. Kuznetsov, *Light: Sci. Appl.* **2022**, *11*, 141.
[17] S. A. Jewell, S. L. Cornford, J. R. Sambles, *J. Appl. Phys.* **2007**, *102*, 093108.
[18] L. De Sio, G. Klein, S. Serak, N. Tabiryan, A. Cunningham, C. M. Tone, F. Ciuchi, T. Bürgi, C. Umeton, T. Bunning, *J. Mater. Chem. C* **2013**, *1*, 7483.
[19] J. Park, J. H. Kang, X. Liu, M. L. Brongersma, *Sci. Rep.* **2015**, *5*, 15754.
[20] J. Park, J. H. Kang, S. J. Kim, X. Liu, M. L. Brongersma, *Nano Lett.* **2017**, *17*, 407.
[21] Y. W. Huang, H. W. Lee, R. Sokhoyan, R. A. Pala, K. Thyagarajan, S. Han, D. P. Tsai, H. A. Atwater, *Nano Lett.* **2016**, *16*, 5319.
[22] G. T. Papadakis, H. A. Atwater, *Phys. Rev. B* **2015**, *92*, 184101.

[23] Y. Li, J. van de Groep, A. A. Talin, M. L. Brongersma, *Nano Lett.* **2019**, *19*, 7988.
[24] K. Xiong, G. Emilsson, A. Maziz, X. Yang, L. Shao, E. W. Jager, A. B. Dahlin, *Adv. Mater.* **2016**, *28*, 9956.
[25] K. Xiong, D. Tordera, G. Emilsson, O. Olsson, U. Linderhed, M. P. Jonsson, A. B. Dahlin, *Nano Lett.* **2017**, *17*, 7033.
[26] K. Xiong, O. Olsson, J. Svirelis, C. Palasingh, J. Baumberg, A. Dahlin, *Adv. Mater.* **2021**, *33*, 2103217.
[27] J. Kim, E. G. Carnemolla, C. DeVault, A. M. Shaltout, D. Faccio, V. M. Shalaev, A. V. Kildishev, M. Ferrera, A. Boltasseva, *Nano Lett.* **2018**, *18*, 740.
[28] J. Kuttruff, D. Garoli, J. Allerbeck, R. Krahne, A. De Luca, D. Brida, V. Caligiuri, N. Maccaferri, *Commun. Phys.* **2020**, *3*, 114.
[29] B. Munkhbat, A. Canales, B. Kucukoz, D. G. Baranov, T. O. Shegai, *Nature* **2021**, *597*, 214.
[30] H. Weir, J. B. Edel, A. A. Kornyshev, D. Sikdar, *Sci. Rep.* **2018**, *8*, 565.
[31] W.-J. Joo, J. Kyoung, M. Esfandyarpour, S.-H. Lee, H. Koo, S. Song, Y.-N. Kwon, S. H. Song, J. C. Bae, A. Jo, M.-J. Kwon, S. H. Han, S.-H. Kim, S. Hwang, M. L. Brongersma, *Science* **2020**, *370*, 459.
[32] J. Zhao, Y. Zhou, Y. Huo, B. Gao, Y. Ma, Y. Yu, *Opt. Express* **2021**, *29*, 23273.
[33] W. Zhang, H. Li, W. W. Yu, A. Y. Elezzabi, *Light: Sci. Appl.* **2020**, *9*, 121.
[34] S. Rossi, O. Olsson, S. Chen, R. Shanker, D. Banerjee, A. Dahlin, M. P. Jonsson, *Adv. Mater.* **2021**, *33*, 2105004.
[35] S. Chen, S. Rossi, R. Shanker, G. Cincotti, S. Gamage, P. Kuhne, V. Stanishev, I. Engquist, M. Berggren, J. Edberg, V. Darakchieva, M. P. Jonsson, *Adv. Mater.* **2021**, *33*, 2102451.
[36] S. Chervinskii, I. Issah, M. Lahikainen, A. R. Rashed, K. Kuntze, A. Priimagi, H. Caglayan, *ACS Appl. Mater. Interfaces* **2021**, *13*, 50564.
[37] S. D. Rezaei, J. Ho, A. Naderi, M. T. Yaraki, T. Wang, Z. Dong, S. Ramakrishna, J. K. W. Yang, *Adv. Opt. Mater.* **2019**, *7*, 1900735.
[38] S. Arif, M. Umar, S. Kim, *ACS Omega* **2019**, *4*, 9010.
[39] D. Chen, T. Wang, G. Song, Y. Du, J. Lv, X. Zhang, Y. Li, L. Zhang, J. Hu, Y. Fu, R. Jordan, *ACS Appl. Mater. Interfaces* **2019**, *11*, 41668.
[40] A. L. Holsteen, S. Raza, P. Fan, P. G. Kik, M. L. Brongersma, *Science* **2017**, *358*, 1407.
[41] A. L. Holsteen, A. F. Cihan, M. L. Brongersma, *Science* **2019**, *365*, 257.
[42] M. Warner, E. M. Terentjev, *Liquid Crystal Elastomers*, Oxford University Press, Oxford, UK **2007**.
[43] P. G. d. Gennes, *C. R. Acad. Sci., Ser. B* **1975**, *281*, 101.
[44] M. Warner, E. M. Terentjev, *Prog. Polym. Sci.* **1996**, *21*, 853.
[45] D. L. Thomsen, P. Keller, J. Naciri, R. Pink, H. Jeon, D. Shenoy, B. R. Ratna, *Macromolecules* **2001**, *34*, 5868.
[46] A. Buguin, M.-H. Li, P. Silberzan, B. Ladoux, P. Keller, *J. Am. Chem. Soc.* **2006**, *128*, 1088.
[47] A. H. Gelebart, D. J. Mulder, M. Varga, A. Konya, G. Vantomme, E. W. Meijer, R. L. B. Selinger, D. J. Broer, *Nature* **2017**, *546*, 632.
[48] J. J. Wie, M. R. Shankar, T. J. White, *Nat. Commun.* **2016**, *7*, 13260.
[49] C. Ohm, M. Brehmer, R. Zentel, *Adv. Mater.* **2010**, *22*, 3366.
[50] M. Tabrizi, T. H. Ware, M. R. Shankar, *ACS Appl. Mater. Interfaces* **2019**, *11*, 28236.
[51] T. H. Ware, M. E. McConney, J. J. Wie, V. P. Tondiglia, T. J. White, *Science* **2015**, *347*, 982.
[52] D. Mistry, M. Nikkhou, T. Raistrick, M. Hussain, E. I. L. Jull, D. L. Baker, H. F. Gleeson, *Macromolecules* **2020**, *53*, 3709.
[53] H. Wermter, H. Finkelmann, *e-Polym.* **2001**, *1*, 013.
[54] D. Martella, S. Nocentini, D. Nuzhdin, C. Parmeggiani, D. S. Wiersma, *Adv. Mater.* **2017**, *29*, 1704047.
[55] H. Zeng, P. Wasylczyk, C. Parmeggiani, D. Martella, M. Burresi, D. S. Wiersma, *Adv. Mater.* **2015**, *27*, 3883.
[56] G. Babakhanova, T. Turiv, Y. Guo, M. Hendrikx, Q. H. Wei, A. Schenning, D. J. Broer, O. D. Lavrentovich, *Nat. Commun.* **2018**, *9*, 456.
[57] D. Liu, D. J. Broer, *Angew. Chem., Int. Ed.* **2014**, *53*, 4542.
[58] J. Küpfer, H. Finkelmnann, *Makromol. Chem., Rapid Commun.* **1991**, *12*, 717.
[59] D. Liu, D. J. Broer, *Langmuir* **2014**, *30*, 13499.
[60] D. J. Broer, R. G. Gossink, R. A. M. Hikmet, *Angew. Makromol. Chem.* **1990**, *183*, 45.
[61] T. J. White, D. J. Broer, *Nat. Mater.* **2015**, *14*, 1087.
[62] A. Komp, J. Rühe, H. Finkelmann, *Macromol. Rapid Commun.* **2005**, *26*, 813.
[63] S. Nocentini, D. Martella, C. Parmeggiani, D. S. Wiersma, *Materials* **2016**, *9*, 525.
[64] I. De Bellis, D. Martella, C. Parmeggiani, E. Pugliese, M. Locatelli, R. Meucci, D. S. Wiersma, S. Nocentini, *J. Phys. Chem. C* **2019**, *123*, 26522.
[65] D. Martella, D. Antonioli, S. Nocentini, D. S. Wiersma, G. Galli, M. Laus, C. Parmeggiani, *RSC Adv.* **2017**, *7*, 19940.
[66] D. Martella, P. Paoli, J. M. Pioner, L. Sacconi, R. Coppini, L. Santini, M. Lulli, E. Cerbai, D. S. Wiersma, C. Poggesi, C. Ferrantini, C. Parmeggiani, *Small* **2017**, *13*, 1702677.
[67] D. Liu, L. Liu, P. R. Onck, D. J. Broer, *Proc. Natl. Acad. Sci. USA* **2015**, *112*, 3880.
[68] H. G. Tompkins, J. N. Hilfiker, *Spectroscopic Ellipsometry: Practical Application to Thin Film Characterization*, Momentum Press, New York, **2015**.
[69] J. Park, J.-H. Kang, A. P. Vasudev, D. T. Schoen, H. Kim, E. Hasman, M. L. Brongersma, *ACS Photonics* **2014**, *1*, 812.
[70] A. Agrawal, B. M. A. Rahman, *Finite Element Modeling Methods for Photonics*, Artech House, London, UK **2013**.
[71] N. Ismail, C. C. Kores, D. Geskus, M. Pollnau, *Opt. Express* **2016**, *24*, 16366.
[72] D. J. Broer, R. A. M. Hikmet, G. Challa, *Makromol. Chem.* **1989**, *190*, 3201.
[73] R. A. M. Hikmet, B. H. Zwerver, D. J. Broer, *Polymer* **1992**, *33*, 89.
[74] M. Taghinejad, W. Cai, *ACS Photonics* **2019**, *6*, 1082.
[75] G. N. Mol, K. D. Harris, C. W. M. Bastiaansen, D. J. Broer, *Adv. Funct. Mater.* **2005**, *15*, 1155.
[76] L. S. Sinev, I. D. Petrov, *Glass Ceram.* **2016**, *73*, 32.
[77] S. Nocentini, D. Martella, C. Parmeggiani, S. Zanotto, D. S. Wiersma, *Adv. Opt. Mater.* **2018**, *6*, 1800167.
[78] S. Nocentini, F. Riboli, M. Burresi, D. Martella, C. Parmeggiani, D. S. Wiersma, *ACS Photonics* **2018**, *5*, 3222.
[79] W. Feng, D. Liu, D. J. Broer, *Small Struct.* **2020**, *2*, 2000107.
[80] H. Zeng, O. M. Wani, P. Wasylczyk, R. Kaczmarek, A. Priimagi, *Adv. Mater.* **2017**, *29*, 1701814.
[81] L. A. A. Pettersson, F. Carlsson, O. Inganäs, H. Arwin, *Thin Solid Films* **1998**, *313–314*, 356.
[82] Y. Xu, R. L. Dupont, Y. Yao, M. Zhang, J.-C. Fang, X. Wang, *Macromolecules* **2021**, *54*, 5376.
[83] Z. Wang, J. K. Lall, Y. Folwill, H. Zappe, *J. Micromech. Microeng.* **2020**, *30*, 075002.
[84] B. Zupančič, B. Zalar, M. Remškar, V. Domenici, *Appl. Phys. Express* **2013**, *6*, 021701.
[85] S. S. Mirshafieyan, H. Guo, J. Guo, *IEEE Photonics J.* **2016**, *8*, 6804912.